Dynamic responses and interactive failure mechanisms of carbon fiber composite face sheets/double-layer corrugated core sandwich structures under low-velocity impacts loading

Hangyan Wang
Xiamen University of Technology

GuangGuang Zhang (✉ zhangguangguang66@163.com)
Xiamen University of Technology

Shuiting Zhou
Xiamen University of Technology

Liange Ouyang
Xiamen University of Technology

Research Article

Dynamic responses and interactive failure mechanisms of carbon fiber composite face sheets/double-layer corrugated core sandwich structures under low-velocity impacts loading

Hangyan Wang[1,2,3,]; Guangguang Zhang[1*] ; Shuiting Zhou[1,2,3]; Liange Ouyang[1,2,3]

1. College of Mechanical and Automotive Engineering, Xiamen University of Technology, Xiamen, Fujian 361024, China

2. Fujian key Laboratory of Advanced Design and Manufacture for Bus & Coach, Fujian 361024, China

3. Key Laboratory of Precision Actuation and Transmission, Fujian Province University, Xiamen 361024, China

ABSTRACT

A single-layer and double-layer corrugated core sandwich structure consisting of carbon fibre–reinforced polymer (CFRP) panels and aluminium alloy core layers was designed. Numerical simulations were carried out in HyperMesh/LsDyna, and the simulation results of single-layer and double-layer corrugated sandwich structure were compared with the experimental results to verify the reliability of the proposed numerical model. Compared with the results of single-layer and double-layer corrugated sandwich structure, the superiority of a double-layer corrugated sandwich structure in anti-collision performance is verified. Considering the effects of impact energy and impact position on impact force, energy absorption capacity, and failure mode, a series of low-velocity impact finite element simulations was carried out. It was found that the main failure mode of composite laminates included fibre damage, matrix damage and delamination, and core buckling. At the same impact position, the higher the impact energy, the greater the initial slopes of the contact force-time and absorbed energy-time curves, the higher the peak force, and the larger the energy absorption capacity. Under the same impact energy, when the impactor hit the wave crest of the sandwich structure, the damage to the structure was small; however, the maximum impact force on the structure was large (~8 kN).

Keywords: Corrugated core sandwich structure, Impact behaviour, Impact force, Energy absorption, Low-velocity impact

1.Introduction

Sandwich structures are prepared by placing a core layer between two panels [1,2,3,4]. These panels mainly provide the tensile and bending resistances to sandwich structures [5,6,7,8], and the core layer bears the transverse shear load [9,10]. The density of lightweight and multifunctional sandwich structures is much lower than that of traditional homogeneous solid materials [11,12,13,14]. The passive safety performance of vehicles can be guaranteed and the lightweight design of vehicles can be realized at the same time through reasonable core layer design and panel layer number optimization [15,16]. However, sandwich structures are vulnerable to low-velocity impacts [17,18,19]. Therefore, extensive research on the low-velocity impact behaviour of sandwich structures is carrying out in recent years [20,21,22].

---

* Corresponding author.

E-mail address: zhangguangguang66@163.com.

Current studies have mainly focused on metallic single-layer corrugated sandwich panels [23]. Some experimental and numerical investigations on single-layer corrugated structures (CF/S-CS) under quasi-static or dynamic/impact loading have been performed [24,25]. He et al. [26] investigated the low-velocity impact characteristics and damage behaviour of hybrid sandwich structures consisting of carbon fibre–reinforced polymer (CFRP) face sheets and aluminium alloy corrugated cores and reported that the slope and peak value of the impact load-time curves increased with the increase in the core thickness and impact energy. Qi et al. [27] investigated the low-velocity impact response of an origami-inspired honeycomb sandwich structure. The results show that the energy absorption characteristics of the origami honeycomb are superior to those of the conventional honeycomb. Bartolozzi et al. [28] performed some static and dynamic experiments to verify the analytical homogenization models for corrugated core sandwich panels. St-Pierre et al. [29] studied the low-velocity impact responses of sandwich beams with a corrugated core or a Y-framed core. Moreover, the effects of panel materials, panel thickness, and core layers on the impact resistance behaviour of sandwich structures have been also explored [30,31]. Zamanifar et al. [32] investigated the mechanical behaviour of corrugated sandwich panels with different size parameters under static and dynamic loading based on the classical finite strip method and propounded that with the increase in the core width, the bending stiffness and shear stiffness of the panels were greatly improved and reduced, respectively. Hou et al. [33] optimized two corrugated sandwich panels with trapezoidal and triangular cores by the explicit finite element technique and reported a close relationship between the deformation process and the crushing force vs time history curves. Wu et al. [34] investigated the effects of core side length and height, impact velocity on the peak load and energy absorption capacity of sandwich structures. The deformation mode, failure mechanism, energy absorption criteria, and optimization design problems of CF/S-CS have been successfully explored. However, single-layer sandwich structures also have some shortcomings. single-layer corrugated structures are prone to the debonding failure of panel and core materials; thus, when such failures occur, their load-bearing capacity gets greatly reduced. Moreover, as core materials generally possess a loose and porous structure, external substances easily penetrate the core through the face panel, leading to the failure of core materials.

To solve the above problems, double-layer sandwich structures (D-CS) consisting of inner and face panels and upper and lower core layers have been designed [35]. An inner panel is used to disperse the concentrated impact effect into the whole structure, resulting in better impact resistance [36]. In addition, double-layer sandwich structures have better designability; thus, they greatly expand the application range of sandwich structures. Hou et al. [37] investigated the mechanical behaviour of multilayer corrugated sandwich panels under quasi-static loading by experiments and numerical simulations and found that the sandwich structure configuration and the number of layers played important roles in the failure mechanism and the energy absorption process. Kilicaslan et al. [38] compared the mechanical responses of single-layer and multilayer corrugated structures with and without aluminium interlayers and reported that multi-layering decreased the buckling stress and increased the densification strain. Cao et al. [39] studied the impact behaviour of multilayer sandwich structures with corrugated cores and revealed the interactions between adjacent layers.

Previous studies have mainly focused on single-layer corrugated structures; therefore, limited research has been performed on the mechanical properties and energy absorption capacity of double-layer sandwich structures. The optimization theories and methods for D-CS are not perfect. Moreover, in comparison to sandwich structures with ordinary metal panels, double-layer

corrugated sandwich structures with fibre-metal-laminated panels have more flexibility. The advantages of fibre-metal-laminated face sheets and double-layer cores need to be exploited to improve the impact resistance of D-CS [40].

The current work mainly investigated the low-velocity impact behaviour and failure mechanisms of D-CS under different impact energies by considering the effects of impact energy and impact position on impact force, energy absorption capacity, and failure mode. Numerical simulations were carried out in HyperMesh/LsDyna software, and the numerical simulation results of CF/S-CS were compared with the low-velocity impact experimental results to verify the reliability of the proposed numerical model. Compared with the numerical simulation results of a double-layer corrugated core sandwich structure, the superiority of CF/D-CS in anti-collision performance is verified.

2. Damage model

2.1 Damage models of intra- and inter-laminar

The main failure modes of composite materials include fibre tensile failure, fibre extrusion failure, matrix cracking, and matrix breakage. The typical multi-mode failure criteria are the Hashin failure criterion, the Chang–Chang failure criterion, and the Hou failure criterion. To simulate the damage of CFRP face sheets under impact loading, a progressive damage model (Material 54/Enhanced Composite Damage Model) based on the Chang–Chang failure criterion is implemented in LSPP. This model points out that the failure of composite materials occurs under the combined action of four different damage and failure forms [41].

In composite laminates, the initiation and propagation of delamination occur under mixed-mode loading. The coupling effect among stress components under different crack modes plays an important role in predicting the initiation and propagation of delamination. Therefore, in this work, the bilinear constitutive model of interface damage initiation and expansion in the mixed-mode was adopted. Fig. 1 displays the bilinear constitutive model of mixed-mode interface damage.
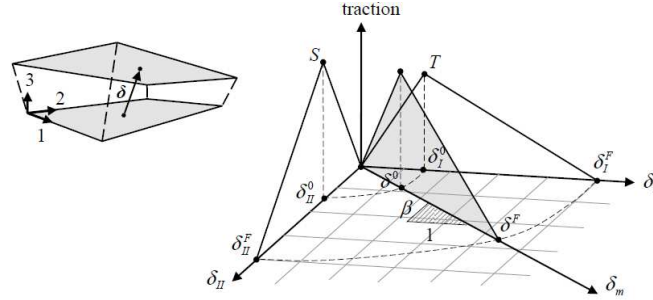

Fig. 1. Mixed-mode traction-separation law

When a structure gets damaged, its elements fail in different forms; thus, a coupling effect occurs between the elements. When the stress component of an element meets the failure criterion, the macro-material properties of the element get weakened. Therefore, different stiffness or strength reduction factors are selected according to different damage forms in the subsequent material performance degradation scheme. However, in the Chang–Chang failure criterion, it is considered that once an element fails, it can no longer bear any load; thus, its stiffness is reduced to zero. In practice, composite materials still have a certain bearing capacity in damaged areas; thus, this model underestimates the strength of composite structures. In the present work, according to different failure modes, the partial degradation model was used to reduce a part of elemental strength to a certain level. The damage evolution process predicted by the Chang–Chang failure model agrees well with experimental results; however, the accuracy depends on the selection of the strength reduction coefficient. According to previous research results [20], the damage models of intra- and

inter-laminar are presented in Table 1. In addition, when an element has different failure modes, its strength degrades continuously.

Table 1. The intra- and inter-laminar damage models

Intralaminar model

Failure modes	Failure criterion	Strength reduction
Tensile fibre failure	$e_f^2 = \left(\dfrac{\sigma_{aa}}{X_t}\right)^2 + \beta\left(\dfrac{\sigma_{ab}}{S_c}\right)$	$X_t = 0.07 X_t$
Compressive fibre failure	$e_c^2 = \left(\dfrac{\sigma_{aa}}{X_c}\right)^2$	$X_c = 0.14 X_c$
Tensile matrix failure	$e_m^2 = \left(\dfrac{\sigma_{bb}}{Y_t}\right)^2 + \left(\dfrac{\sigma_{ab}}{S_c}\right)^2$	$Y_t = 0.2 Y_t$
Compressive matrix failure	$e_d^2 = \left(\dfrac{\sigma_{bb}}{2S_c}\right)^2 + \left[\left(\dfrac{Y_c}{2S_c}-1\right)^2\right]\dfrac{\sigma_{bb}}{Y_c} + \left(\dfrac{\sigma_{ab}}{S_c}\right)^2$	$X_c = 0.4 X_c$

Interlaminar and interface model

Failure criterion	Damage evolution criterion	Mix-mode fracture energy criterion
$\left(\dfrac{\langle t_n\rangle}{t_n^0}\right)^2 + \left(\dfrac{t_s}{t_s^0}\right)^2 + \left(\dfrac{t_t}{t_t^0}\right)^2$	$D = \dfrac{\delta_m^f\left(\delta_m^{\max}-\delta_m^0\right)}{\delta_m^{\max}\left(\delta_m^f-\delta_m^0\right)}$	$G^C = G_n^C + (G_s^C - G_n^C)\left(\dfrac{G_s}{G_T}\right)^\eta$

where e_f, e_c, e_m, e_d are damage factors corresponding to four failure modes. σ_{aa}, σ_{bb}, σ_{ab} are the effective stress. X_t, X_c, Y_t, Y_c, S_c are fiber, matrix and shear strengths, respectively. E_a, E_b are the longitudinal and transverse Young's modulus, respectively. G_{ab} is the shear modulus ab. β is adopted to control the nonlinear term of shear stress on fiber tension mode. For $\beta = 1$, we get the original criterion of Hashin [1980] in the tensile fiber mode. For $\beta = 0$, we get the maximum stress criterion which is found to compare better to experiments [41]. $\langle\ \rangle$ represents the Macaulay bracket operator, which has the relation of $\langle\alpha\rangle = (\alpha + |\alpha|)/2$. G^C, $G_S = G_s + G_t$ and $G_T = G_n + + G_s + G_t$ are fracture energy parameters.

2.2 Damage model of aluminium alloys

According to Johnson and Cook(J-C) , the flow stress can be expressed as

$$\sigma_y = \left(A + B\bar{\varepsilon}^{p^n}\right)\left(1 + C\ln\dot{\varepsilon}^*\right)\left(1 - \frac{T - T_{room}}{T_{melt} - T_{room}}\right)^m \qquad (1)$$

where A, B, C, and n are input constants; $\bar{\varepsilon}^p$ is the effective plastic strain; and T, T_{room}, and T_{melt} are the current temperature, the reference temperature (generally room temperature = 293 K), and the melting point, respectively. In the above formula, the first term on the right-hand side reflects the quasi-static stress–strain relationship of aluminium alloys, the second term indicates the enhancement effect of strain rate on alloy strength (strain rate effect), and the third term reflects the softening effect of temperature on alloy strength (temperature effect).

In order to avoid mesh distortion caused by excessive material deformation under large impacts, the J-K model uses a damage parameter (D) to measure the damage mode of aluminium alloys. When the damage parameter is equal to 1, aluminium alloys fail.

$$D = \sum\frac{\Delta\bar{\varepsilon}^p}{\varepsilon^f} \qquad (2)$$

where ε^f is the fracture strain.

$$\varepsilon^f = \left[D_1 + D_2\exp D_3\sigma^*\right] + \left[1 + D_4\ln\dot{\varepsilon}^*\right] + \left[1 + D_5 T^*\right] \qquad (3)$$

4

where σ^* is the ratio of pressure and the effective stress.

$$\sigma^* = \frac{p}{\sigma_{eff}} \qquad (4)$$

where p is the hydrostatic pressure and σ_{eff} is the equivalent stress.

3. Experimental study

3.1 Specimen preparation

Two types of corrugated sandwich structures (CF/S-CS and CF/D-CS) with a size of 96 mm × 96 mm × 15.65 mm were prepared. Fig. 2 displays the schematic diagrams of the two structures. CF/S-CS was made from an aluminium alloy corrugated core and two carbon fibre–reinforced polymer (CFRP) face sheets, whereas CF/D-CS consisted of two aluminium alloy sheets and two carbon fibre–laminated core layers. The CFRP face sheets (T700/3234) with an average thickness of 1 mm were fabricated in a stacking sequence of [0°, 90°, 0°, 90°]. The aluminium alloy core (2A12-T4) had three unit cells with a thickness of 0.8 mm. The Double-layer corrugated structure was constructed by sequentially assembling aluminium trapezoidal cores (Fig. 2). The material properties of the unidirectional laminates are listed in Table 2. The material properties of the aluminium alloy sheets are presented in Table 3, and their plastic stress–strain curve is displayed in Fig. 3.
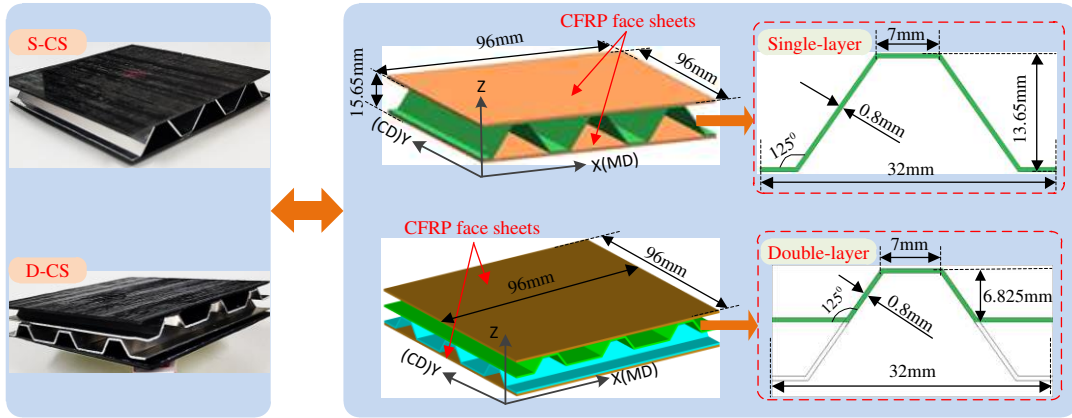

Fig. 2. Schematic diagrams of corrugated sandwich structures

Table 2. Material properties of unidirectional laminates (T700/3234) [26]

Symbol	Property	Value
ρ	Mass density	1560kg/m3
E_{11}	Longitudinal stiffness	123GPa
E_{22}	Transverse stiffness	8.4 GPa
υ_{12}	Poisson's ratio	0.32
G_{12}, G_{13}	Shear modulus	4 GPa
G_{23}	Shear modulus	3 GPa
X^T	Longitudinal tensile strength	2100 MPa
X^C	Longitudinal compressive strength	800 MPa
Y^T	Transverse compressive strength	25 MPa
Y^C	Transverse tensile strength	120 MPa
S^L, S^T	Shear strength	40 MPa
N	Normal interface failure strength	56 MPa
S, T	Shear interface failure strength	70 MPa
G_{1C}	Normal energy release rate	0.504 kJ/m2

| G_{2C} | Shear energy release | 1.1 kJ/m^2 |

Table 3. Material properties of aluminium alloy sheets (2A12-T4)

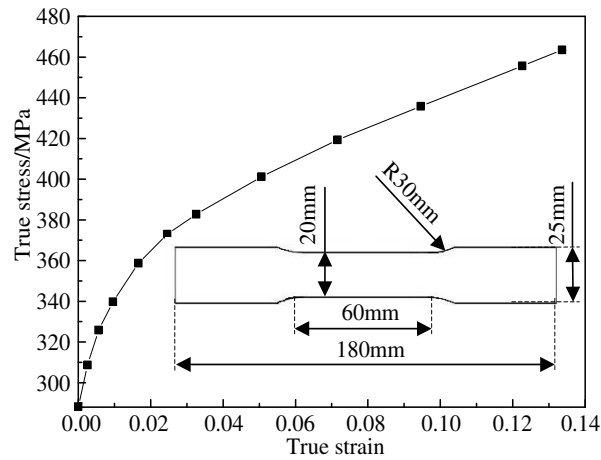| Mass density	Young's modulus	Poisson's ratio	Yield strength
2700 kg/m^3	70 GPa	0.3	464 MPa

Fig. 3. Tensile stress–strain curve of 2A12-T4 aluminium alloy

3.2 Impact tests

In order to verify the feasibility of the numerical modelling method proposed in this work, a low-velocity impact test was conducted on CF/S-CS and CF/D-CS by a drop hammer tester (Fig. 4). The specimen was inserted between the impactor and a rigidly supported plate. There was a 34 mm width long hole in the middle of the clamps base. The specimens were placed into the clamps, and the degrees of freedom on both sides of the specimen are constrained through the bolt screw locking mechanism of the clamps. The impactor had a hemisphere shape with a diameter of 12 mm, and a counterweight of 13.2 kg was used. The impact energy was 10 J, and according to the law of energy conservation, the corresponding initial impact velocity was 1.23 m/s. Corrugation peaks were selected as impact positions to explore their influences on the impact behaviour of CF/S-CS and CF/D-CS.
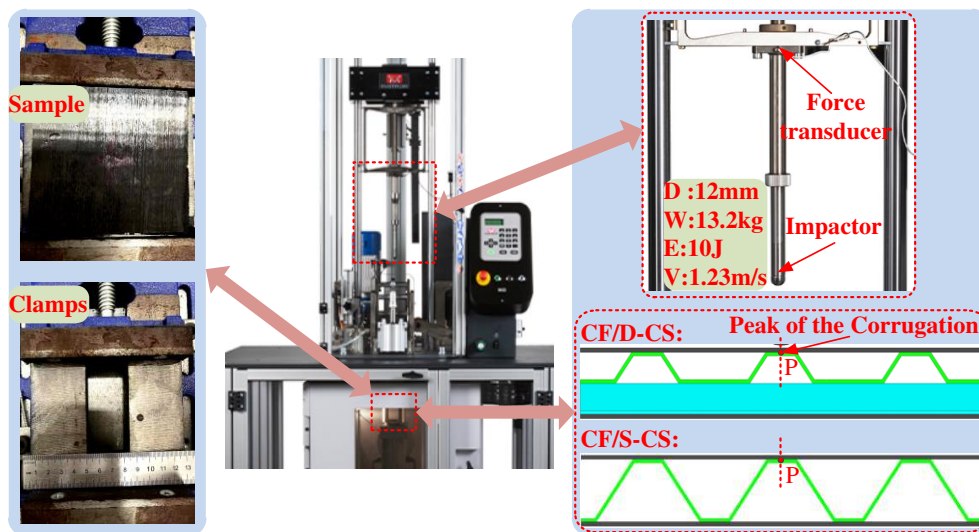

Fig. 4. Experimental setup for the CF/S-CS and CF/D-CS impact test

6

3.3 Numerical investigation

3.3.1 Finite element model

The finite element model for low-velocity impact simulations is presented in Fig. 5. The CFRP face sheets were modelled using MAT 54 material in LS-DYNA, and a progressive failure model for solid elements was developed based on the modified Chang–Chang failure criterion to predict tensile and compressive fibre failures and tensile and compressive matrix failures (Table 1). The panel was meshed using hexahedral solid elements, and the impact area was meshed encrypted with dimensions of 0.5mm × 0.5mm. The core was meshed using quadrilateral Belytschko–Tsay shell elements, and the MAT_JOHNSON_COOK material model (MAT 15) was used to model the aluminium alloy (2A12-T4). An 'AUTOMATIC_SURFACE_TO_SURFACE_TIEBREAK' contact was used to bond the core layers and the panels. An 'AUTOMATIC_SURFACE_TO_SURFACE' contact was defined between the indenter and the upper panel. An 'AUTOMATIC_SINGLE SURFACE' contact was considered to simulate the self-contact of the core sheets during deformation.

The lower clamps were made of ordinary steel. In order to keep consistency with the test boundary conditions, the clamps with a long hole of 34 mm width in the middle was set at the lower ends of the corrugated sandwich structure. The impactor was modelled as a rigid body with a mass of 13.2 kg. The material properties of solid elements were Young's modulus (E) = 210 GPa, Poisson's ratio (v) = 0.3, and density (q) = 7800 kg/m^3. Four impact energies of 10 J, 20 J, 40 J, and 50 J with the corresponding initial velocities of 1.23 m/s, 1.74 m/s, 2.46 m/s, and 2.75 m/s, respectively, were adopted to conduct the low-velocity impact simulations of CF/D-CS. The coding process for the low-velocity impact simulations is depicted in Fig. 6.
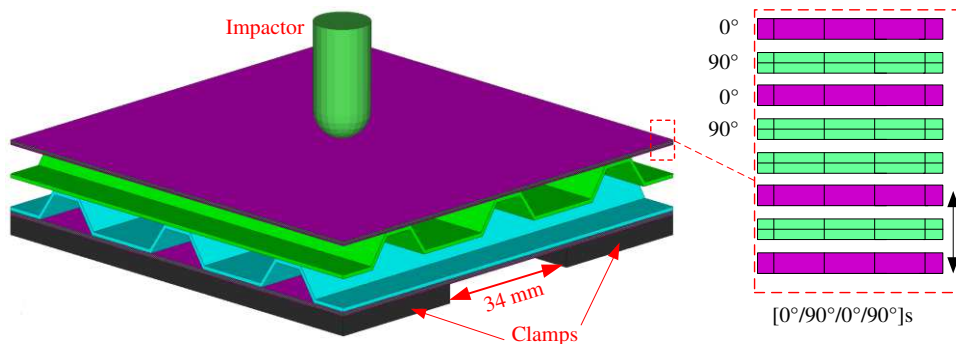

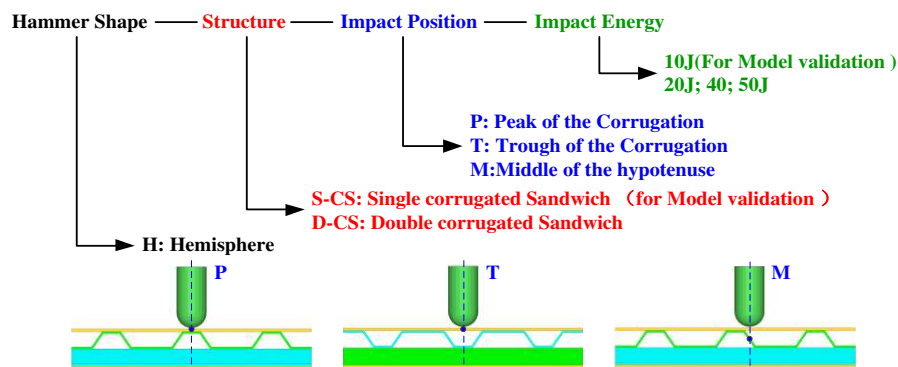Fig. 5. Finite element model for low-velocity impact simulations

Fig. 6. Coding process of the finite element model

3.3.2 Model validation

In this paper, the drop hammer impact tests of short-span CF/D-CS and CF/S-CS specimens with an impact energy of 10J are carried out, and the numerical results are compared with the experimental results to verify the feasibility of the finite element model. Fig.7 and Fig.8 compares the contact force and energy absorption curves extracted from both the testing and numerical computation of CF/D-CS and CF/S-CS specimens under 10 J impact energies. It is shown that the simulated force–time curves coincide well with the experiment, as evidenced by the agreement between the simulation and experimental data of both peak force and response time. The impact process can be divided into three stages.

Stages1: Once the punch touches the upper panel, the impact force starts to increase approximately linearly. The core material and the upper panel jointly bear the impact load until the core web buckles and the impact force reaches the peak at t=2.7ms; Stages2: The core material and the upper panel jointly bear the impact load, and the core material undergoes plastic deformation, and the impact force enters a stable fluctuation period, at which the plastic deformation of the core layer and the upper panel connection area increases, and the force does not continue to increase, and the impact force basically remains the same at t=2.7~4.05ms. Stages3: When the impact force and punch depth reach the maximum, the punch speed drops to zero and the punch starts to rebound until the punch is completely disconnected from the specimen (t=4.05~8ms), and the impact process ends. Eventually the upper panel showed less obvious fracture and delamination damage of the Fibres (shown in Fig. 9), the core layer is pitted at the connection area with the upper panel, and the core layer web is deformed by power flexure.
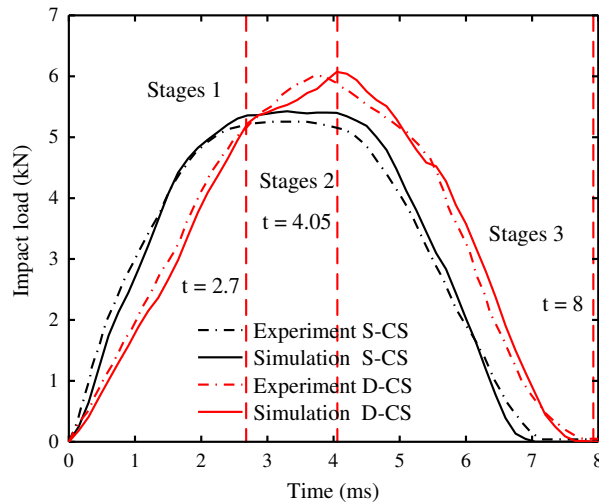

Fig. 7. Force-time curves of CF/S-CS and CF/D-CS under 10-J impact energy

It is noticeable from the absorbed energy-time curves shown in Fig. 8 that during the low-speed impact, the kinetic energy of the impactor was converted into the internal energy of the corrugated sandwich structure at t=0~4 ms; hence, the curve rapidly reached the peak, and almost all the kinetic energy of the impactor was absorbed. Subsequently, the impactor started to rebound, and the elastic strain energy of the corrugated sandwich structure was converted into the kinetic energy of the impactor at t=4~8 ms, in turn, the curve gradually decreased to a stable value. Therefore, the final energy conversion was accompanied by the partial conversion of the kinetic energy of the impactor into the internal energy (mainly plastic strain energy) of the corrugated sandwich structure. The maximum energy is expressed as E_{max}, the absorbed energy is expressed as E_{ab}, and the rebound
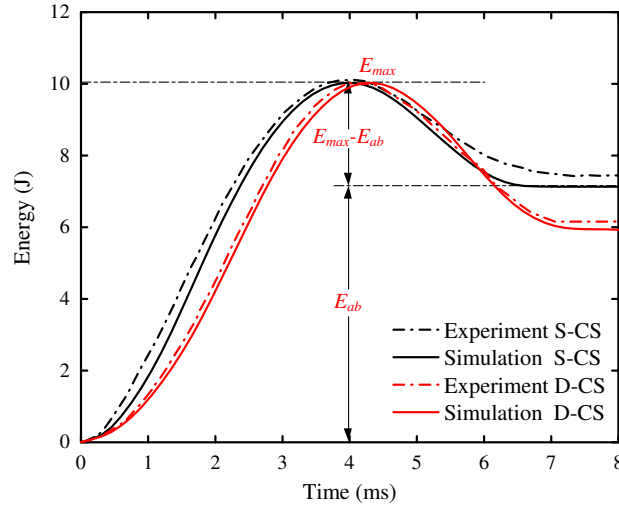
energy is expressed as E_{max}-E_{ab}.

Fig. 8. Absorbed energy-time curves of CF/S-CS and CF/D-CS under 10 J impact energy

It is evident that the impact forces on both CF/S-CS and CF/D-CS increased linearly at the beginning of the impact process and decreased rapidly to zero after reaching the peak. However, the force-displacement curve slope for CF/D-CS at the beginning of the impact process was smaller than that of CF/S-CS, the time to reach the peak impact force for CF/D-CS was later than that of CF/S-CS, the peak impact force of CF/D-CS was greater than that of CF/S-CS, and the plateau stabilization zone of CF/D-CS was smaller than that of CF/S-CS (CF/D-CS had almost no plateau stabilization zone). As the internal space of CF/S-CS was larger, the web of its core layer buckled and lost the load-bearing capacity; hence, the impact was mainly resisted by the short edge of the corrugated core and the upper carbon fibre panel. Now, changing CF/S-CS to CF/D-CS by keeping the height between the upper and lower panels the same made the internal space of the structure smaller and the stiffness larger. Hence, the flexural load-carrying capacity increased and could withstand larger impact loads. At the impact energy of 10 J, both CF/S-CS and CF/D-CS could resist the impact and the kinetic energy of the impactor was completely absorbed. However, the rebound velocity of the impactor for CF/D-CS was higher than that for CF/S-CS. It happened because the deformation energy absorption capacity of the upper panel mainly concentrated in the span of the impacted single cell; thus, the difference in the span distance caused the difference in the energy absorption capacity of the upper panel, whereas the difference in the deformation failure mode caused the difference in the energy absorption capacity of the core layer. CF/D-CS had a larger single span and a smaller internal space, and higher stiffness than CF/S-CS; thus, the rebound speed of the impactor for CF/D-CS was higher.

3.3.3 Reinforcement and coupling deformation mechanisms

Fig. 9 compares the deformation and damage patterns of CF/S-CS and CF/D-CS obtained from the numerical investigation under 10-J impact energy. It is noticeable that the indentation under the impactor was almost invisible on the top panel of the specimens and the bottom panel of the specimens was not damaged. The load-time curves of the specimens under 10-J impact energy were relatively smooth, implying that the CFRP panels had less damage and the corrugated core experienced less plastic deformation. No significant difference between the final damage patterns of CF/S-CS and CF/D-CS was detected due to the small impact energy. The main failure modes for both structures were the delamination failure between the panels and the core layer and the buckling

9

of the core. The aluminium alloy core web experienced flexural deformation and bulging, and the corrugated core layers remained in the plastic deformation state.
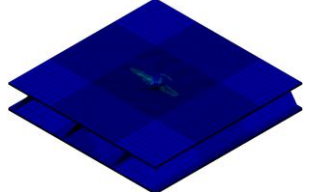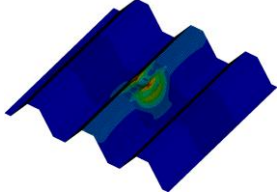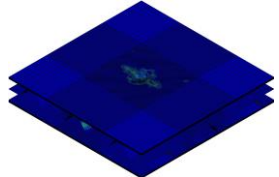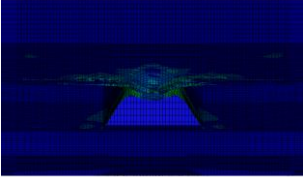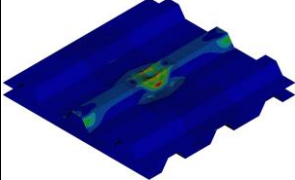
Specimen		Top surface	Cross-section	Core
CF/S-CS	Experiment			
	Simulation			
CF/D-CS	Experiment			
	Simulation			

Fig. 9. Final failure modes of CF/S-CS and CF/D-CS under 10 J impact energy

Therefore, the simulation results of CF/S-CS and CF/D-CS (peak load and the damage and deformation patterns of the panels and the core layers) were well consistent with the experimental ones. The results implying that the proposed finite element model could be adopted to simulate the mechanical behaviour of corrugated sandwich structures.

## 4. Numerical analysis of CF/D-CS under low-velocity impacts

The proposed numerical model was used to further explore the mechanical properties, energy absorption capacity, and damage modes of CF/D-CS under different low-velocity impact energies.

4.1 Dynamic responses of CF/D-CS at the peak impact position

4.1.1 Contact force and energy absorption capacity

The contact force and energy absorption curves of CF/D-CS at the peak of the hemispherical hammer shock wave are displayed in Figs. 10(a) and 10(b), respectively. With the increase in impact energy, the slope and peak of both the contact force-time and absorbed energy-time curves increased; thus, the contact time during the impact process was extended. When the corrugated sandwich structure wave crest was subjected to a greater shock load, the contact time between the impactor and the upper panel got longer, the impact displacement of the impactor was greater, and the structure absorbed more energy and got severely damaged. The contact force-time curves of CF/D-CS at 10 J and 20 J were flatter than those at 40 J and 50 J due to the relatively smaller impact energies and the less damage to the structure. The contact force-time curves of CF/D-CS reached the peak at about 4 ms for both the impact energies of 10 J and 20 J and then decreased linearly to zero at around 8 ms. When the impact energies were 40 J and 50 J, the contact force reached the peak at about 2 ms due to the higher impact energy, the faster impact speed, and the shorter time

required to reach the critical point of structural damage, then dropped for a short time, became stabilized for a short time, and finally, continued to decrease. When the impact energy was 50 J, the impactor penetrated the top panel and the upper corrugated core; thus, the lower corrugated core became loaded, and the contact force dropped to zero after fluctuating at about 4.5 kN. When the impact energies were 10 J, 20 J, 40 J, and 50 J, the corrugated sandwich structure resisted the impact and completely absorbed the kinetic energy of the impactor, and subsequently, it rebounded (Fig. 10(b)). During the rebound process, a part of the elastic strain energy of the corrugated sandwich structure was converted into the kinetic energy of the impactor, and subsequently, the absorbed energy-time curves gradually decreased to a stable value.
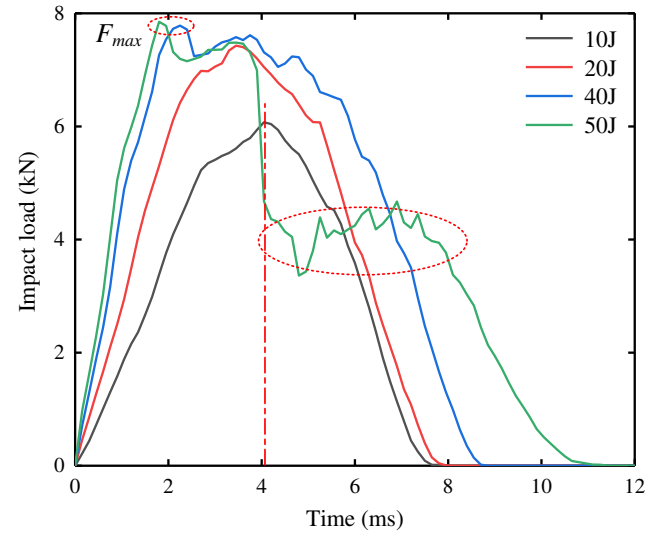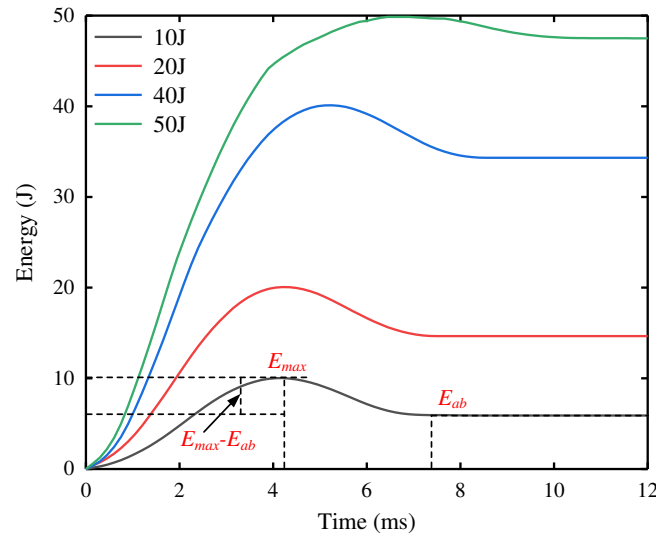
(a) Contact force

(b) Energy absorption

Fig. 10. Contact force-time curve and absorbed energy-time curve of the corrugated sandwich structure at the peak impact position

Fig. 11 presents the peak forces and energy absorption indexes of the sandwich structure under different impact loads (calculated from the contact force and energy absorption curves shown in Fig. 10). When the hemispherical hammer shock wave reached the peak, the peak force increased by 22.4%, 28.2%, and 29.3%, respectively, as the impact energy increased from 10 J to 20 J, 40 J, and 50 J. Therefore, the higher the impact load, the greater the peak force; however, the difference in

the peak forces was small because the corrugated sandwich structure wave crest was resisted by the upper corrugated core under the impact load. When the impact energies were 10 J, 20 J, 40 J, and 50 J, the sandwich structure absorbed approximately 59%, 73.25%, 85.8%, and 95% of the impact energy, respectively. According to the energy absorption index, the greater the impact energy, the higher the absorbed energy by the interlayers of the sandwich structure. As the sandwich structure was not damaged at the low-energy impact, more elastic strain energy of the structure was converted into the kinetic energy of the impactor; thus, the final absorbed energy by CF/D-CS was smaller.
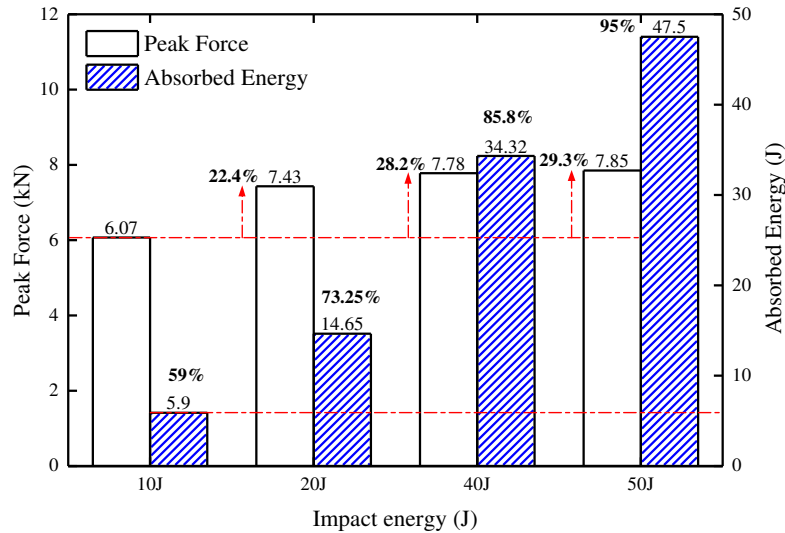

Fig. 11. Peak forces and energy absorption indexes of CF/D-CS under different impact energies

4.1.2 Damage failure modes

The stress distributions in the top panel, core layer, and cross-section of CF/D-CS and the damage pattern of the composite laminates are exhibited in Fig. 12, where the rainbow colour represents the degree of damage to the composite panel, the white area indicates that the element that appeared to be overly deformed was removed, the red area indicates that the material was severely damaged, the blue area indicates no damage, and the other areas indicate different degrees of damage. Under the 10 J impact, no cracks appeared in the top panel and the core and only indentation deformation occurred. In the cross-section, the core web experienced dynamic buckling deformation. The main failure modes were fibre breakage and matrix damage. Under the 20 J impact, a small opening was created in the top panel, the core layer web also experienced indentation deformation, and the damaged area was significantly enlarged. Under the 40 J and 50 J impacts, perforations (circular holes) were formed in the top panel. At the higher impact energy of 50 J, these holes were more regular and the upper core layer failed with the extension of the metal crack. The main damage patterns were still fibre fracture and matrix damage. As the impact energy increased, the damage got more severe and the damaged area significantly increased. In all cases, no damage to the bottom panel was noticed.

		Top surface		Core	Cross-section
10J impact event	Stress distribution				
	D	Fibre tension	Fibre compression	Matrix tension	Matrix compression

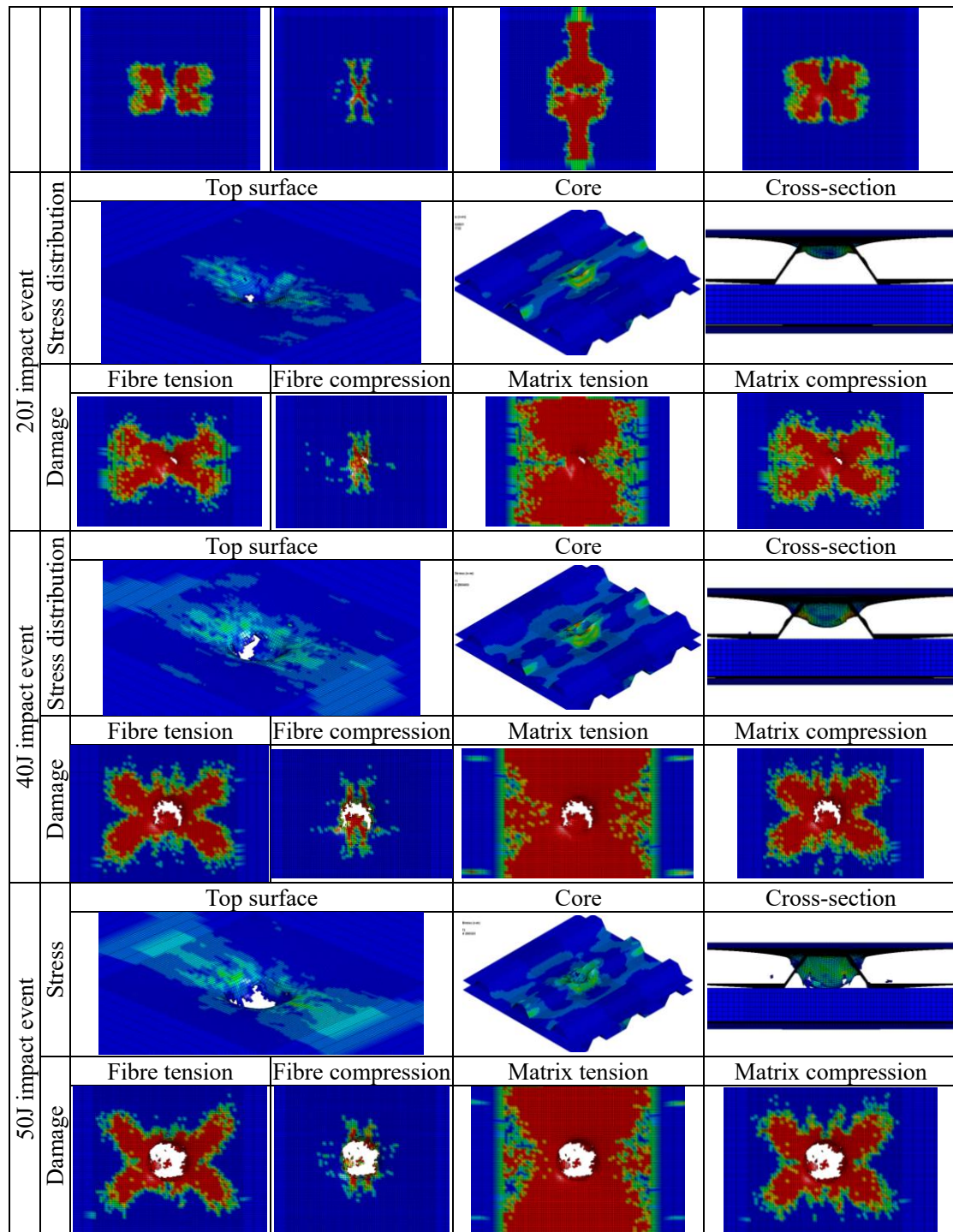|		Top surface	Core	Cross-section
20J impact event	Stress distribution			
		Fibre tension	Fibre compression	Matrix tension	Matrix compression
	Damage				
40J impact event	Stress distribution	Top surface	Core	Cross-section
		Fibre tension	Fibre compression	Matrix tension	Matrix compression
	Damage				
50J impact event	Stress	Top surface	Core	Cross-section
		Fibre tension	Fibre compression	Matrix tension	Matrix compression
	Damage				

Fig. 12. Stress and damage distributions in CF/D-CS at the peak impact position

4.2 Dynamic responses of CF/D-CS at the impact position on the trough

4.2.1 Contact force and energy absorption capacity

Figs. 13(a) and 13(b) display the contact force and energy absorption curves of CF/D-CS, respectively, when the hemispherical hammer impacted the trough of the sandwich structure. With the increase in impact energy, the slope and peak value of both the contact force-time and absorbed energy-time curves increased. When the wave trough of the corrugated sandwich structure was subjected to a large impact load, the impactor speed got faster and the structure absorbed more energy and got severely damaged. The contact force-time curves at 10 J and 20 J were flatter than

those at 40 J and 50 J because the impact energy was relatively smaller and the structure was less damaged. It was found that the larger the impact energy, the higher the degree of damage. In addition, the contact-time curves at 10 J, 20 J, and the other two impact energies, respectively, had one peak point, two peak points, and three peak points. The first peak point of the contact force curves under the four impact energies was detected around 3 kN. When the impactor hit the top panel, the contact force rapidly increased; thus, the top panel experienced serious damage, and circular holes were formed in it. The contact force-time curve at 10 J slowly decreased to zero after reaching the first peak value, indicating that the impact energy was completely absorbed by the top panel. At the impact energy of 20 J, the impactor continued to punch the upper core layer, in turn, the aluminium alloy core layer buckled. Consequently, the contact force reached the second peak value, the punch started to rebound, and the contact force linearly decreased to 0 kN. At the impact energies of 40 J and 50 J, the impactor broke through the upper core layer and the contact force dropped significantly until the impactor hit the lower core layer and then increased to the third peak.

When the impact energies were 10 J, 20 J, 40 J, and 50 J, the corrugated sandwich structure resisted the impact and the kinetic energy of the impactor was completely absorbed, in turn, the structure started to rebound (Fig. 13(b)). The energy absorption curves at 10 J, 20 J, and the other two impact energies had one stage, two stages, and three stages, respectively. In the first stage, the top panel resisted the shock wave and absorbed a part of the kinetic energy. In the second stage, the top panel fractured and lost its resistance to failure; thus, the aluminium alloy core became the main impact load-bearing component. In the third stage, the first and second aluminium alloy cores jointly absorbed the impact energy after buckling. In the rebound process, a part of the elastic strain energy of the corrugated sandwich structure was converted into the kinetic energy of the impactor and the remaining energy was absorbed by the corrugated sandwich structure. Consequently, the absorbed energy-time curve gradually decreased to a stable value.
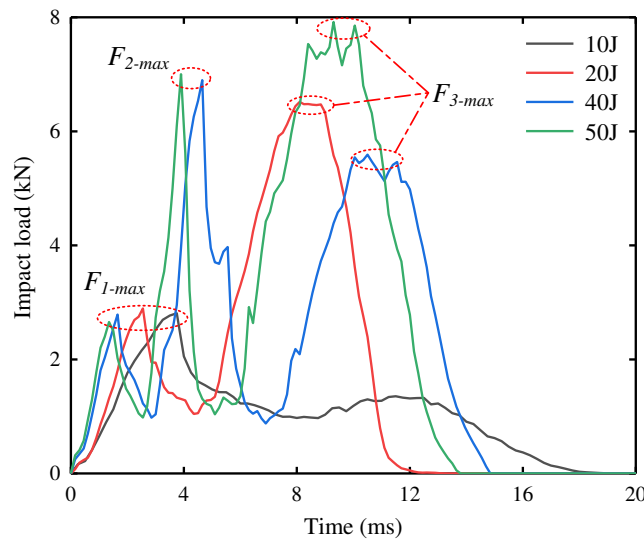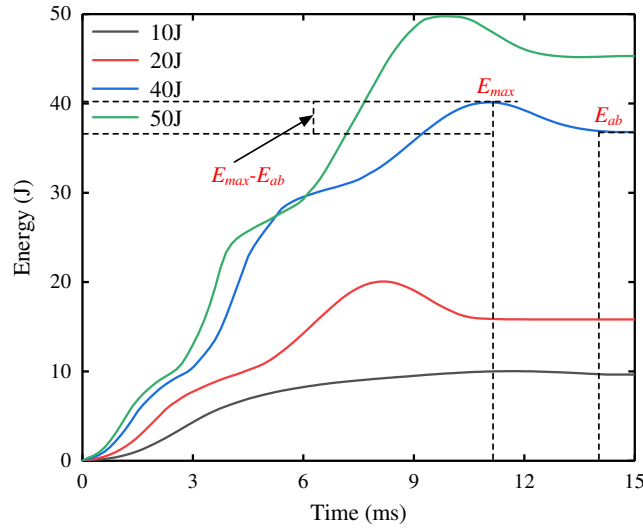
(a) Contact force

(b) Energy absorption

Fig. 13. Contact force-time curve and absorbed energy-time curve of the corrugated sandwich structure at the impact position on the trough

Fig. 14 presents the peak forces and energy absorption indexes of the sandwich structure under different impact loads (calculated from the contact force and energy absorption curves shown in Fig. 13). When the hemispherical hammer impacted the trough, the peak force increased by 131.67%, 145.55%, and 181.85%, respectively, as the impact energy increased from 10 J to 20 J, 40 J, and 50 J. The higher the impact load, the greater the peak force. Under the 10-J impact, the impactor did not touch the aluminium alloy core layer; hence, the contact force was very small. The difference in contact forces under the other three impact loads was small. When the impact energies were 10 J, 20 J, 40 J, and 50 J, the sandwich structure absorbed about 94.6%, 79.1%, 92%, and 90.6% of the impact energy, respectively. When the impact energy was 20 J, the deformation of the aluminium alloy core was recovered and more elastic strain energy was converted into the kinetic energy of the impactor; thus, the absorbed energy by the sandwich structure was lower than those under the other three impact energies.
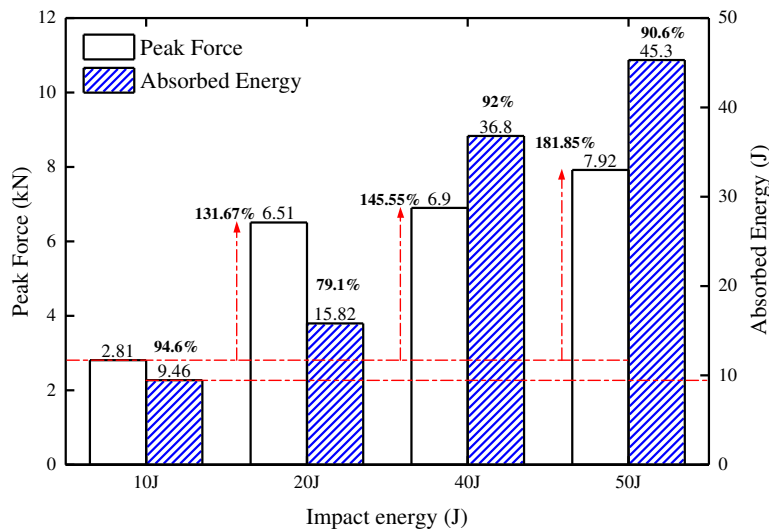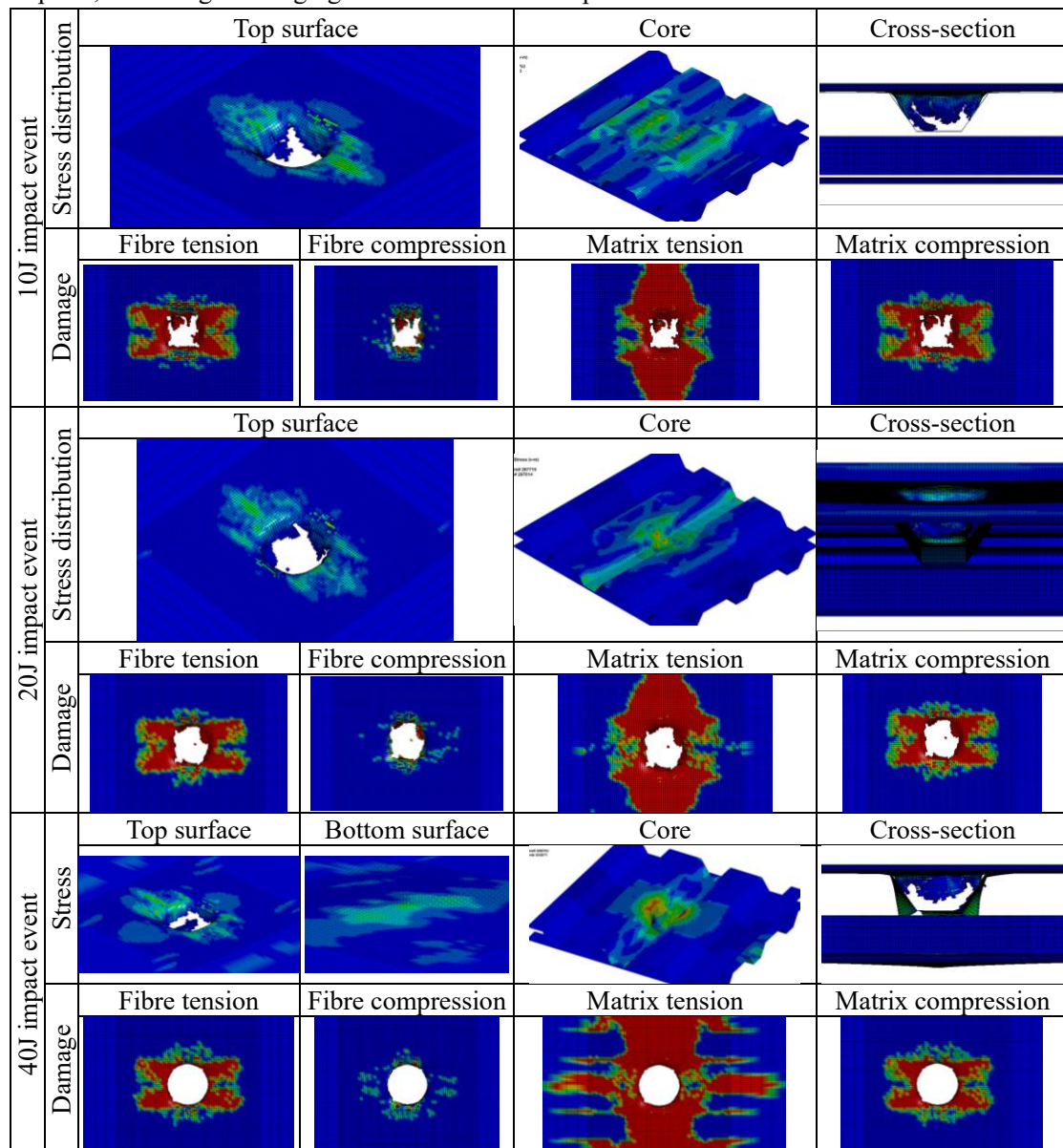

Fig. 14. Peak forces and energy absorption indexes of CF/D-CS under different impact energies

4.2.2 Damage failure modes

The stress distribution and damage mode of CF/D-CS at the impact position on the trough under different impact energies are displayed in Fig. 15. Under the 10 J and 20 J impacts, perforations (circular holes) appeared in the top panel and the main failure modes were fibre fracture and matrix damage. When the impactor hit the upper core layer at 20 J, the core layer got slightly depressed. Under the 40 J and 50 J impacts, the impactor broke through the top panel and hit the upper core layer. The failure of the upper core layer causes the crack to expand and formed an opening, and the bottom panel had different degrees of bulging. The fibre fracture and matrix compression areas remained the same under the 10 J and 20 J impacts; however, the matrix damage area increased at 20 J. The bulging of the bottom panel at 50 J was more severe than that at 40 J. under the four impact energies, the fibre damage areas and stress distributions of CF/D-CS were similar. It because when the CF/D-CS trough was impacted, top panel below the impact point and the short edge of the core layer are not directly supported, forming a blank area, and top panel resists the impact under load, so the top panel first appears round hole failure and absorbs impact energy. Under 10 J and 20 J impacts, no damage or bulging noticed in the bottom panel.

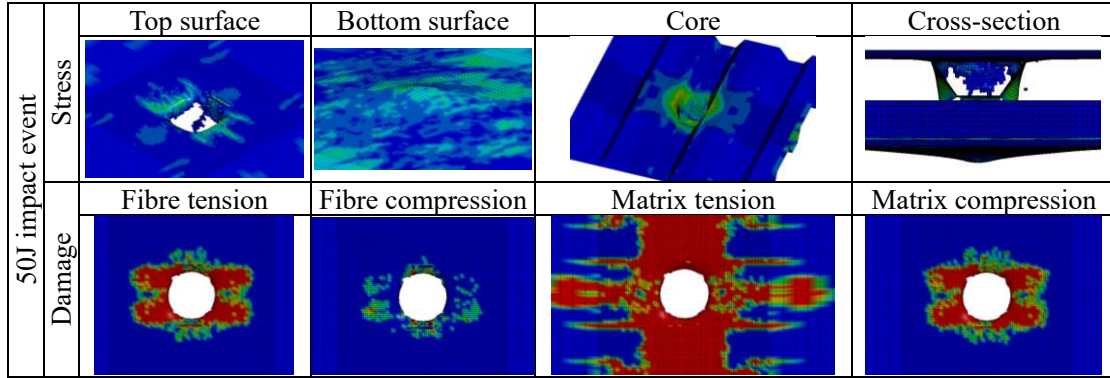|		Top surface	Bottom surface	Core	Cross-section
50J impact event	Stress				
		Fibre tension	Fibre compression	Matrix tension	Matrix compression
	Damage				

Fig. 15. Stress and damage distributions in CF/D-CS at the impact position on the trough

4.3 Dynamic responses of CF/D-CS at the impact position in the Middle of the hypotenuse

4.3.1 Contact force and energy absorption capacity

The contact force and energy absorption curves of CF/D-CS are displayed in Figs. 16(a) and 16(b), respectively, when the hemispherical hammer impacted at the middle of the peak and trough of the corrugated sandwich structure. With the increase in impact energy, the slope and peak value of the contact force-time and absorbed energy-time curves increased; thus, the contact time in the impact process was prolonged. When a large impact load acted at the middle of the peak and trough of the corrugated sandwich structure, the impactor broke through the top panel and got in contact with the bevelled edge of the core layer; hence, the impact depth of the puncher became large, and the structure absorbed more energy and got severely damaged. The contact force-time curves of the structure at 10 J and 20 J were smooth because under the relatively smaller impact energies, only the top panel was destroyed and the sandwich structure was not damaged.

The contact force-time curves of the structure at 40 J and 50 J were similar. When the contact force reached the first peak point, the contact force-time curve decreased slightly, then rapidly reached the second peak, again decreased rapidly, and finally, increased slowly to the third peak. The first peak represents the bearing capacity of the carbon fibre–laminated top panel before it got seriously damaged. The second peak represents the contact force induced by the impactor when it got in contact with the inclined edge of the upper core layer after the failure of the carbon fibre–laminated top panel; thus, the corrugated sandwich structure became the main impact load-bearing component. The third peak represents the maximum contact force produced by the oblique edge of the lower core layer after the buckling of the upper core layer. Subsequently, the puncher started to rebound, and the contact force was linearly reduced to 0 kN. When the impact energies were 10 J, 20 J, 40 J, and 50 J, the corrugated sandwich structure resisted the impact and completely absorbed the kinetic energy of the impactor, causing a springback phenomenon (Fig. 16(b)). In the rebound process, a part of the elastic strain energy of the corrugated sandwich structure was converted into the kinetic energy of the impactor and the curve gradually decreased to a stable value.
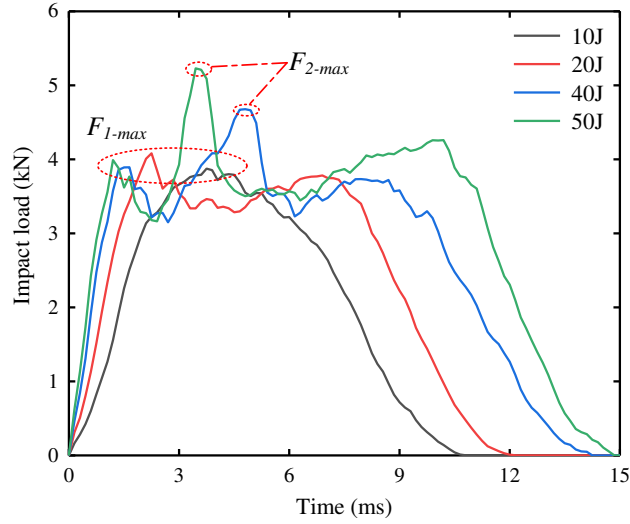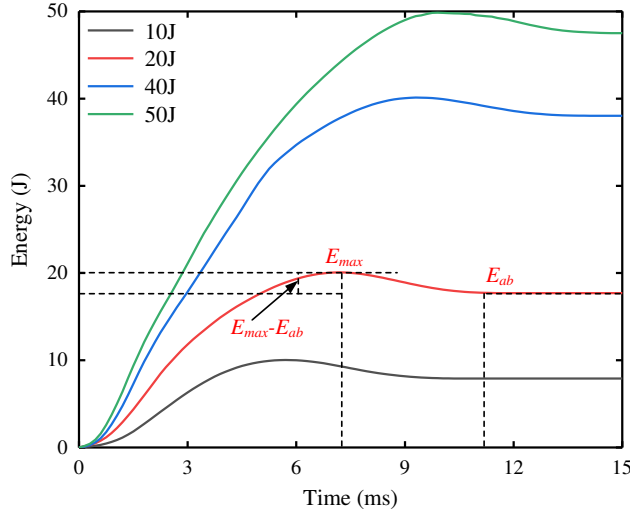
(a) Contact force

Fig. 16. Contact force-time curve and absorbed energy-time curve of CF/D-CS at the impact position in the middle of the peak and the trough

Fig. 17 presents the maximum contact forces and energy absorption indexes of the sandwich structure under different impact loads (calculated from the contact force and energy absorption curves shown in Fig. 16). When the hemispherical hammer hit the middle of the wave crest and trough of the sandwich structure, the peak force increased by 5.15%, 20.62%, and 34.79%, respectively, when the impact energy increased from 10 J to 20 J, 40 J, and 50 J. When the sandwich structure was subjected to a high impact load, a large contact force was generated between the puncher and the structure. When the impact energies were 10 J, 20 J, 40 J, and 50 J, the sandwich structure absorbed about 79.1%, 88.5%, 95.08%, and 95.02% of the impact energy, respectively. It was found that the greater the impact energy, the higher the absorbed energy of the sandwich structure.
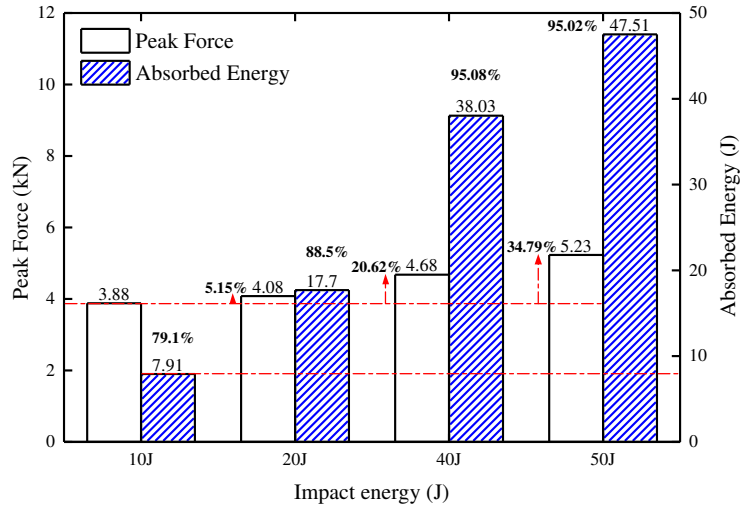
Fig. 17. Peak forces and energy absorption indexes of CF/D-CS under different impact energies

4.3.2 Damage failure modes

The stress distribution and damage mode of CF/D-CS under different impact energies are presented in Fig. 18, when the hemispherical hammer impacted at the middle of the peak and the trough. Under the 10-J impact, the top panel had a small crack, the core web experienced a slight sunken deformation, and the main failure modes were fibre fracture and matrix damage. Under the 20-J impact, a circular hole appeared in the top panel, the impactor broke through the panel and hit the upper core, and the core web also collapsed. The failure modes under the 40-J and 50-J impacts were similar. The impactor penetrated the top plate and formed a circular hole and then impacted the upper core layer. The extension of the crack formed a petal-like opening in the upper core. However, under the 40-J impact, the lower core layer only experienced a slight bending deformation, and under the 50-J impact, the depression deformation of the lower core got more serious, generating a crack opening at the joint between the oblique edge and the short edge. The fibre fracture and matrix damage areas of the top panel under different impact energies were almost the same. Due to the impact at the middle of the bevelled edge, the top panel was supported by the shorter side of the upper core layer on the left side of the impact point; thus, the fibre fracture propagated vertically on the left side of the circular hole and was extended diagonally on the right side. In all cases, no damage to the bottom panel was noticed; thus, the stress distribution and damage mode of the bottom panel are not presented in Fig. 18.

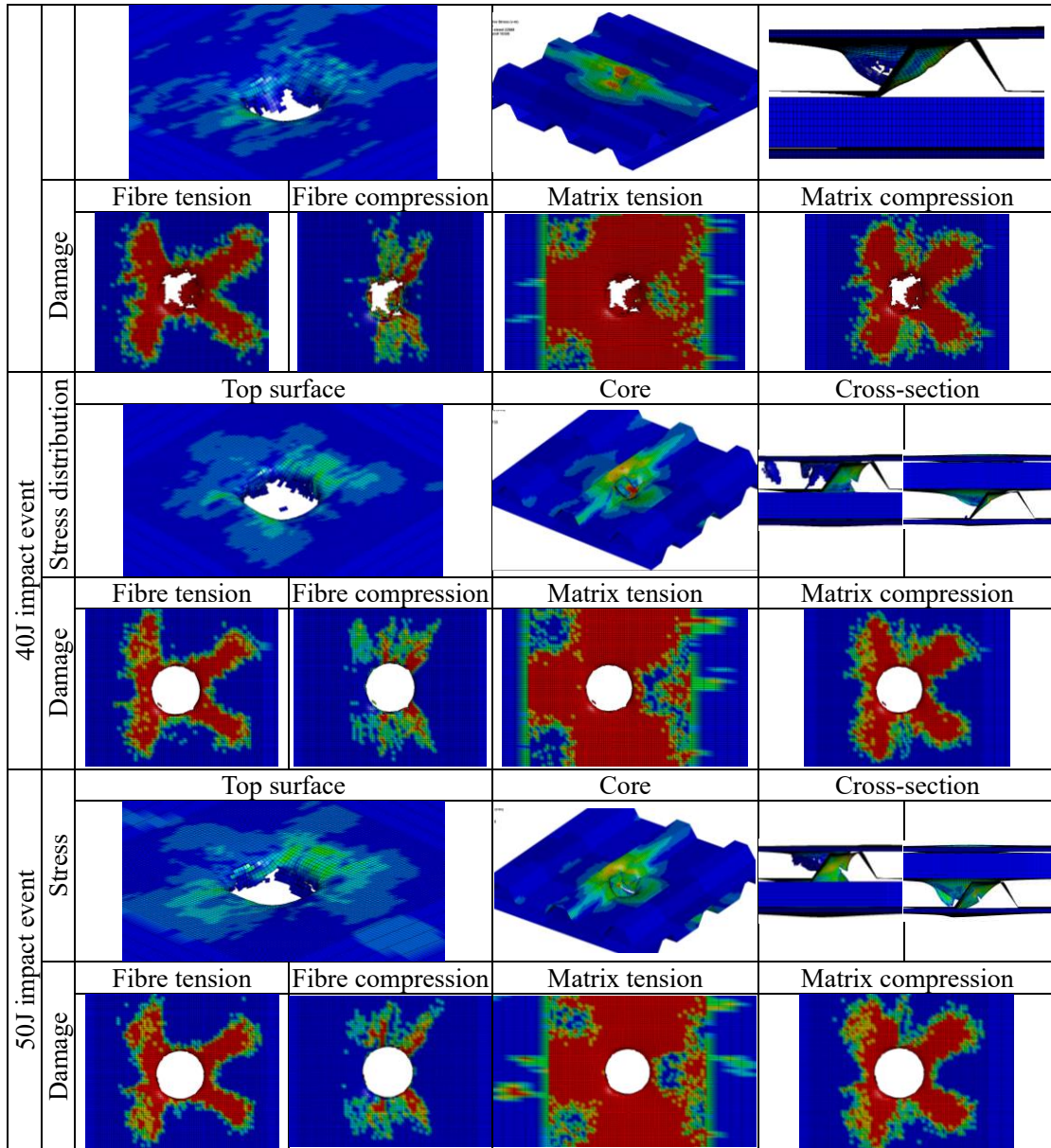|					
		Fibre tension	Fibre compression	Matrix tension	Matrix compression
	Damage				
40J impact event	Stress distribution	Top surface		Core	Cross-section
		Fibre tension	Fibre compression	Matrix tension	Matrix compression
	Damage				
50J impact event	Stress	Top surface		Core	Cross-section
		Fibre tension	Fibre compression	Matrix tension	Matrix compression
	Damage				

Fig. 18. Stress and damage distributions in CF/D-CS at the impact position in the middle of the peak and the trough

5. Conclusion

The low-velocity impact response and impact damage of single-layer and double-layer corrugated core sandwich structure consisting of carbon fibre–reinforced polymer panels and aluminium alloy core layers were experimentally and numerically investigated. In order to better explore the impact resistance of the structure, considering the effects of impact energy and impact position on impact force, energy absorption capacity, and failure mode, a series of low-velocity impact finite element simulations was carried out. The main observations of this work are drawn below.

(1) Under low-velocity impacts, the double-layer corrugated sandwich structure manifested excellent energy absorption performance by exploiting the tensile properties of fibre material. The main failure modes included fibre tensile fracture, fibre delamination, and matrix damage. Circular holes were formed in the carbon fibre–reinforced polymer panels, and crack propagation in the aluminium alloy core caused a petal-opening failure.

(2) At the same impact position, the higher the impact energy, the greater the initial slopes of the

contact force-time and absorbed energy-time curves, the higher the peak force, and the larger the energy absorption capacity.

(3) Under the same impact energy, when the hammer hit the peak of the corrugated sandwich structure, the panels and the aluminium alloy core were slightly damaged because they jointly bore the impact load. However, as the hammer did not break through the structure at lower energies, the aluminium alloy core absorbed the impact energy through depression deformation and started to rebound. In the rebound process, more elastic strain energy of the corrugated sandwich structure was converted into the kinetic energy of the impactor; thus, the structure absorbed less energy at low impact energies.

(4) Under the same impact energy, when the impact occurred on the trough of the structure, a smaller peak force of about 2.8 kN was generated. When the impact occurred on the wave crest of the structure, the largest peak force of about 8 kN was recorded. However, when the impact occurred between the peak and trough of the corrugated sandwich structure, the peak force was the smallest and the energy absorption capacity was the largest.

Acknowledgment

Data Availability

The raw/processed data required to reproduce these findings cannot be shared at this time as the data also forms part of an ongoing study.

Declaration of Competing Interest

The authors declare that they have no known competing financial interests or personal relationships that could have appeared to influence the work reported in this paper.

References

[1] Oliazadeh P , Farshidianfar A , Crocker M J . Experimental study and analytical modeling of sound transmission through honeycomb sandwich panels using SEA method. Composite Structures, 2022, 280:114927.

[2] Harvey D , Hubert P . 3D topology optimization of sandwich structures with anisotropic shells. Composite structures, 2022(Apr.):285.

[3] White R , Machavaram V R , Fernando B A , et al. Vertically-aligned short E-glass fibre core sandwich composite: Production and evaluation. Journal of Sandwich Structures and Materials, 2022, 24(1):174-200.

[4] Hu GL, Shen YC, Fan QL, Zhao WL, Liu TY, Ma CR, Jia CL, Liu M. Improved Leakage Behavior at High Temperature via Engineering of Ferroelectric Sandwich Structures. Materials, 2023, 16(2).

[5] Huang H , Yang X , Yan Q , et al. Crashworthiness analysis and multiobjective optimization of bio-inspired sandwich structure under impact load. Thin-Walled Structures, 2022, 172:108840.

[6] Ebo-Quansah I , Hassanin A H , Adachi T , et al. Ballistic Testing Simulation of Ultra-High Strength Steel Water Layer Sandwich Structure. Materials Science Forum, 2022.

[7] Wang T , Guo L . A realistic model for transverse shear stiffness prediction of composite corrugated-core sandwich structure with bonding effect. Journal of Sandwich Structures and Materials, 2022, 24(1): 763-788.

[8] Ferdous W, Manalo A, Aravinthan T, Fam A. Flexural and shear behaviour of layered sandwich beams. Constr Build Mater 2018;173:429–42.

[9] Jiang HY, Ren YR, Zhang SJ, Liu ZH, Yu GQ, Xiang JW. Damage and perforation resistance behaviors induced by projectile impact load on bonding-patch repaired and scarf-patch repaired composite laminates. Int J Damage Mech 2019;28:502-37.

[10] Han B, Qin KK, Yu B, Wang B, Zhang QC, Lu TJ. Honeycomb–corrugation hybrid as a novel sandwich core for significantly enhanced compressive performance. Mater Design 2016;93:271-82.

[11] Wang H, Xie H. Multi-objective optimization of crashworthiness of vehicle front longitudinal beam. Struct Multidiscip O 2020;61:2111-23.

[12] Boonkong T, Shen YO, Guan ZW, Cantwell WJ. The low velocity impact response of curvilinear-core sandwich structures. Int J Impact Eng 2016;93:28–38.

[13] Cai ZB, Li ZY, Ding Y, Zheng J, Liu JH, Zhou ZR. Preparation and impact resistance performance of bionic sandwich structure inspired from beetle forewing. Compos Part B Eng 2019;161:490–501.

[14] Yu K, Hu H, Tang H, Giunta G, Potier-Ferry M, Belouettar S. A novel twodimensional finite element to study the instability phenomena of sandwich plates. Comput Method Appl M 2015;283:1117-37.

[15] Yang XF, Ma JX, Shi YL, Sun YX, Yang JL. Crashworthiness investigation of the bio-inspired bi-directionally corrugated core sandwich panel under quasi-static crushing load. Mater Design 2017;135:275-90.

[16] Sun GY, Chen DD, Wang HX, Hazell PJ, Li Q. High-velocity impact behaviour of aluminium honeycomb sandwich panels with different structural configurations. Int J Impact Eng 2018; 122:119-36.

[17] Chen DY, Yan RJ, Lu X. Mechanical properties analysis of the naval ship similar model with an integrated sandwich composite superstructure. Ocean Eng 2021;232:109101.

[18] Ivanez I, Moure MM, Garcia-Castillo SK, Sanchez-Saez S. The oblique impact response of composite sandwich plates. Compos Struct 2015;133:1127-36.

[19] Dayyani I, Shaw AD, Flores ELS, Friswell MI. The mechanics of composite corrugated structures: a review with applications in morphing aircraft. Compos Struct 2015;133:358–80.

[20] Liu Q, Xu XY, Ma JB, Wang JS, Shi Y, Hui D. Lateral crushing and bending responses of CFRP square tube filled with aluminum honeycomb. Compos Part B Eng 2017;118:104-15.

[21] Taraghi I, Fereidoon A. Non-destructive evaluation of damage modes in nanocomposite foam-core sandwich panel subjected to low-velocity impact. Compos Part B Eng, 2016;103:51-59.

[22] Qin QH, Zhang W, Liu SY, Li JF, Zhang JX, Poh LH. On dynamic response of corrugated sandwich beams with metal foam-filled folded plate core subjected to low-velocity impact. Compos Part A: Appl Sci Manuf 2018;114:107–16.

[23] Jiang HY, Ren YR, Jin QD, Zhu GH, Liu ZH. Flexural performances of fiber face-sheets/corrugated core sandwich composite structures reinforced by horizontal stiffeners. Int J Mech Sci 2020;168.

[24] Wang X, He C, Yue ZS, Li X, Yu RP, Ji HB, Zhao ZY, Zhang QC, Lu TJ. Shock resistance of

elastomer-strengthened metallic corrugated core sandwich panels. Compos Part B Eng 2022;237.

[25] Li FH, Han B, Zhang Q C, Jin F, Lu TJ. Buckling of a standing corrugated sandwich plate subjected to body force and terminal load. Thin-Wall Struct 2018;127:688-99.

[26] He WT, Liu JX, Tao B, Xie D, Liu JY, Zhang M. Experimental and numerical research on the low velocity impact behavior of hybrid corrugated core sandwich structures. Compos Struct 2016;158:30-43.

[27] Qi J , Li C , Ying T , et al. Energy absorption characteristics of origami-inspired honeycomb sandwich structures under low-velocity impact loading. Materials & Design, 2021.

[28] Bartolozzi G, Baldanzini N, Pierini M, Zonfrillo G. Static and dynamic experimental validation of analytical homogenization models for corrugated core sandwich panels. Compos Struct 2015;125:343-53.

[29] St-Pierre L, Deshpande V S, Fleck N A. The low velocity impact response of sandwich beams with a corrugated core or a Y-frame core. Int J Mech Sci. 2015;91:71-80.

[30] Liu Q, Xu XY, Ma JB, Wang JS, Shi Y, Hui D. Lateral crushing and bending responses of CFRP square tube filled with aluminum honeycomb. Compos Part B Eng 2017;118:104-15.

[31] Mondal S , Patra A K , Chakraborty S, Mitra N. Dynamic performance of sandwich composite plates with circular hole/cut-out: A mixed experimental–numerical study. Compos Struct 2015; 131:479-89.

[32] Zamanifar H, Sarrami-Foroushani S, Azhari, M. Static and dynamic analysis of corrugated-core sandwich plates using finite strip method. Eng Struct 2019;183:31-50.

[33] Hou SJ, Zhao SY, Ren LL, Han X, Li Q. Crashworthiness optimization of corrugated sandwich panels. Mater Design 2013;51:1071-84.

[34] Wu YH, Qiang L, Fu J, Li Q, Hui D. Dynamic crash responses of bio-inspired aluminum honeycomb sandwich structures with CFRP panels. Compos Part B Eng 2017;121:122-33.

[35] Pydah, A, Batra RC. Analytical solution for cylindrical bending of two-layered corrugated and webcore sandwich panels. Thin-Walled Struct 2018;123:509-19.

[36] Zhou XS , Mei ZY , Zhang YB. Low-velocity impact response and energy dissipation mechanism of composite multilayer array structures – Experimental and finite element analysis. Compos Struct 2018;197:89-105.

[37] Hou SJ, Shu CF, Zhao SY, Liu TY, Han X, Li Q. Experimental and numerical studies on multi-layered corrugated sandwich panels under crushing loading. Compos Struct 2015;126:371-85.

[38] Kilicaslan C, Guden M, Odaci IK, Tasdemirci A. Experimental and numerical studies on the quasi-static and dynamic crushing responses of multi-layer trapezoidal aluminum corrugated sandwiches. Thin-Walled Struct 2014;78:70-78.

[39] Cao BT, Hou B, Li YL, Zhao H. An experimental study on the impact behavior of multilayer sandwich with corrugated cores. Int J Solid Struct 2017;109:33-45.

[40] Bikakis GSE, Dimou CD, Sideridis EP. Ballistic impact response of fiber-metal laminates and monolithic metal plates consisting of different aluminum alloys. Aerosp Sci Technol 2017;69:201-08.

[41] LSTC LD (2003) Keyword User's Manual.Version,960, 1-2.

Supplementary Files

This is a list of supplementary files associated with this preprint. Click to download.

- GraphicalAbstract.pdf